NONLINEAR MAGNETOHYDRODYNAMICS: NUMERICAL CONCEPTS

R. Keppens
FOM Institute for Plasma Physics Rijnhuizen, Association Euratom-FOM
P.O. Box 1207, 3430 BE Nieuwegein, The Netherlands

ABSTRACT

The ideal MagnetoHydroDynamic (MHD) equations accurately describe the macroscopic dynamics of a perfectly conducting plasma. Adopting a continuum, single fluid description in terms of the plasma density ρ, velocity $\mathbf{v}$, thermal pressure p and magnetic field $\mathbf{B}$, the ideal MHD system expresses conservation of mass, momentum, energy, and magnetic flux. This nonlinear, conservative system of 8 partial differential equations enriches the Euler equations governing the dynamics of a compressible gas with the dynamical influence – through the Lorentz force – and evolution – through the additional induction equation – of the magnetic field $\mathbf{B}$. In multi-dimensional problems, the topological constraint expressed by the Maxwell equation $\nabla \cdot \mathbf{B} = 0$, represents an additional complication for numerical MHD. Basic concepts of shock-capturing high-resolution schemes for computational MHD are presented, with an emphasis on how they cope with the thight physical demands resulting from nonlinearity, compressibility, conservation, and solenoidality.

I. LINEAR ADVECTION PROBLEM

As a preliminary to the full Euler and MHD system addressed below, it is instructive to focus on a seemingly trivial problem at first, namely the numerical solution to the advection equation in 1 spatial (x) dimension given by

$$\partial_t \rho + v \partial_x \rho = 0. \tag{1}$$

Under a constant given velocity v, an initial density pulse $\rho(x, t = 0) = \rho_0(x)$ will merely be advected at the constant speed, such that $\rho(x, t) = \rho_0(x - vt)$. Analytically, we are done.

Numerically, we need to discretize the problem both spatially and temporally, and come up with a recipe to advance the discrete solution ρ_i^n on grid cells indexed by i from time level t_n to t_{n+1}. A forward Euler temporal discretization, combined with a centered difference spatial gradient approximation, suggests as a time-stepping recipe:

$$\frac{\rho_i^{n+1} - \rho_i^n}{\Delta t} + v \frac{\rho_{i+1}^n - \rho_{i-1}^n}{2\Delta x} = 0. \tag{2}$$

Unfortunately, this method leads unavoidably to a numerical instability, under all combinations of time step Δt and grid size Δx. This can be predicted by a Von Neumann stability analysis of the discrete formula (2), which inserts $\rho(x, t_n) = G^n \rho_o e^{ikx}$ and computes the amplification factor $\mid G \mid$ defined from $\rho^{n+1} = \frac{G^{n+1}}{G^n} \rho^n \equiv G\rho^n$. The unconditional instability of the method is found from $\mid G \mid > 1$ for all wavenumbers k.

Luckily, there are several ways to 'cure' the instability (at least conditionally) by slightly modifying the formula (2). One way is to replace the centered difference spatial gradient by a one-sided gradient operator, taken in the 'upwinded' direction. That is, if the flow goes from left to right ($v > 0$), simply use the upwind scheme

$$\frac{\rho_i^{n+1} - \rho_i^n}{\Delta t} + v \frac{\rho_i^n - \rho_{i-1}^n}{\Delta x} = 0. \tag{3}$$

A method which mixes spatially forward and backward differences as follows

$$\begin{aligned} \rho_i^* &= \rho_i^n - \frac{\Delta t}{\Delta x} v \left(\rho_{i+1}^n - \rho_i^n \right) \\ \rho_i^{**} &= \rho_i^n - \frac{\Delta t}{\Delta x} v \left(\rho_i^* - \rho_{i-1}^* \right) \\ \rho_i^{n+1} &= \frac{\rho_i^* + \rho_i^{**}}{2} \end{aligned} \tag{4}$$

is known as the MacCormack method, and this can be rewritten as

$$\begin{aligned} \rho_i^{n+1} &= \rho_i^n - \frac{\Delta t}{\Delta x} v \left(\frac{\rho_{i+1}^n - \rho_{i-1}^n}{2} \right) \\ &\quad + \frac{(\Delta t)^2}{(\Delta x)^2} v^2 \left(\frac{\rho_{i+1}^n - 2\rho_i^n + \rho_{i-1}^n}{2} \right). \end{aligned} \tag{5}$$

Hence, while the upwind method (3) stabilizes the scheme (2) by replacing the centered spatial gradient with a one-sided one, the MacCormack scheme in effect adds a 'diffusive' type term. Note that for the constant coefficient linear advection problem (1) considered here,

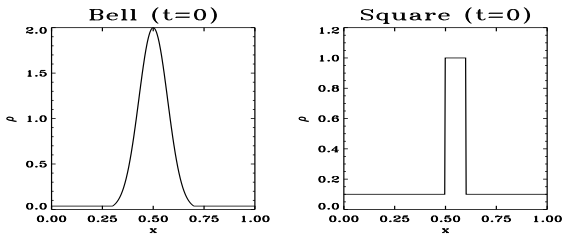

Figure 1: Initial data for periodic advection problems: Gaussian bell and square pulse

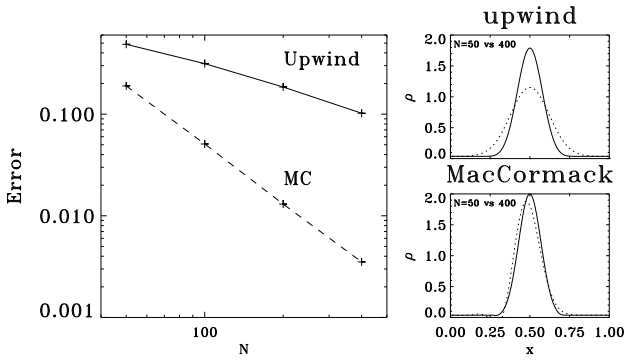

Figure 2: Error versus number of grid points for periodic advection of a smooth bell profile. Upwind method (solid) versus MacCormack method (dashed). Representative solutions are at right.

the method (5) is also referred to as a Lax-Wendroff scheme. A third option to stabilize the scheme (2) is to replace the ρ_i^n in the temporal gradient approximation by a centered average, namely

$$\rho_i^{n+1} = \frac{1}{2}(\rho_{i+1}^n + \rho_{i-1}^n) - \frac{\Delta t}{2\Delta x} v(\rho_{i+1}^n - \rho_{i-1}^n). \qquad (6)$$

This scheme is known as the Lax-Friedrichs discretization. Performing a Von Neumann stability analysis on any of the three modifications (3,5,6), one obtains the following condition for stability $\Delta t \leq \Delta x/v$. For a chosen grid size Δx, this condition on the time step will apply generally to any explicit time stepping scheme where future ρ_i^{n+1} values are directly computable from presumed known values ρ_i^n at time level t_n.

As a numerical example, we simulate the periodic advection of a smooth Gaussian bell profile as well as an initial square pulse (with 2 discontinuities). The initial data is shown in Fig. 1 and the side boundaries $x = 0$ and $x = 1$ are treated periodically. Since the analytical solution is known, we can easily compute the true error as a function of resolution. This is done after one full advection cycle of the Gaussian profile for both the upwind and the MacCormack scheme for resolutions $[50, 100, 200, 400]$, as shown in Fig. 2. Representative solutions are depicted as well. For this smooth

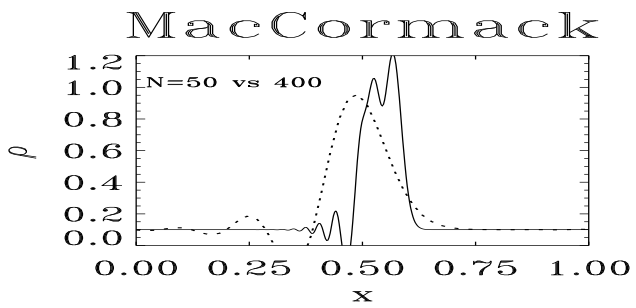

Figure 3: Two solutions (50 grid points, dotted; 400 points, solid) of the periodic advection of the square pulse from Fig. 1. Results for the MacCormack scheme after one full advection cycle.

initial data, the MacCormack scheme renders second order accuracy, while the upwind scheme is only first order accurate, as evident in the slope of the error versus grid number curve. Obviously, the first order upwind scheme suffers from rather large numerical diffusion as the bell profile widens. The Lax-Friedrichs scheme (6) is also only first order accurate. However, with the square pulse as initial data, a similar exercise will show that the MacCormack scheme falls back to first order accuracy as well. We show in Fig. 3 two numerical solutions after 1 advection cycle for the pulse: the MacCormack scheme is clearly dispersive and therefore suffers from the oscillatory Gibbs phenomenon at the discontinuities. These linear advection experiments are indicative for numerical simulations of more physical systems: a wish for high order accuracy on smooth data, as well as a desire to avoid the introduction of spurious oscillations in discontinuous profiles will in fact call for nonlinearity in the discretization methods employed.

II. EULER SYSTEM AND RANKINE-HUGONIOT

The governing conservation laws for the 1D dynamics of a compressible gas are the Euler equations, written as

$$\begin{cases} \rho_t + (\rho\, v)_x &= 0 \\ m_t + (m\, v + p)_x &= 0 \\ e_t + (e\, v + p\, v)_x &= 0 \end{cases} \qquad (7)$$

The vector of conserved quantities $U = (\rho\, m\, e)$ contains the density ρ, momentum $m = \rho v$, and total energy density computed from

$$e = \underbrace{\frac{\rho v^2}{2}}_{\text{kinetic}} + \underbrace{\frac{p}{\gamma - 1}}_{\text{thermal energy}} ,$$

with the ratio of specific heats γ entering as a parameter. This system can be written as $U_t + (F(U))_x = 0$

when we introduce the flux vector

$$F(U) = \begin{pmatrix} m \\ \frac{m^2}{\rho}\frac{3-\gamma}{2} + (\gamma-1)e \\ \frac{em}{\rho}\gamma - \frac{\gamma-1}{2}\frac{m^3}{\rho^2} \end{pmatrix}$$

The Euler system allows for discontinuous solutions where a constant left state $U_l = (\rho_l\, m_l\, e_l)$ is separated from a constant right state $U_r = (\rho_r\, m_r\, e_r)$ by jumps in the conserved quantities at a location which travels at a 'shock speed' s. Such a traveling discontinuity must still obey the discrete equivalent of the conservation laws, expressed by the Rankine-Hugoniot relation

$$F(U_l) - F(U_r) = s\,(U_l - U_r)\,. \tag{8}$$

Note that for a given right state, this constitutes a system of 3 equations for 4 unknowns, namely s and U_l. In particular, a contact discontinuity which travels at the fluid velocity $s = v$ and only carries an arbitrary jump in density $\rho_l \neq \rho_r$, while having constant velocity $v_l = v_r = v$ and constant pressure $p_l = p_r = p$, is a viable solution to the Euler system. Hence, the numerical treatment of these contact discontinuities in gas dynamic simulations already calls for a scheme which appropriately deals with advection problems of discontinuous profiles.

Apart from the contact discontinuities, genuine shock solutions are obtained from the relations (8). Writing the system of conservation laws as a quasilinear system with the flux Jacobian $\partial F/\partial U \equiv F_U$, we get

$$U_t + F_U U_x = 0.$$

The 3×3 flux Jacobian matrix has 3 distinct (right) eigenvector/eigenvalue pairs, where the eigenvalues are given by

$$\begin{aligned} \lambda_1 &= v - c \\ \lambda_2 &= v \\ \lambda_3 &= v + c, \end{aligned} \tag{9}$$

where the sound speed $c = \sqrt{\gamma p/\rho}$ enters. The eigenvalues of the flux Jacobian are closely connected with the Rankine-Hugoniot system (8). In particular, when the initial condition for an Euler simulation consists of two constant states U_l and U_r separated by a discontinuity – known as the Riemann problem, these will generally not allow for a single shock speed s obeying the Rankine-Hugoniot relations. Instead, out of the contact point of the initial two constant states, 3 'wave' signals will emerge separating 4 constant states. The two emergent intermediate states U_{ml} and U_{mr} will be connected by a contact discontinuity traveling at the speed v_* which is identical for these two states (as is the intermediate pressure p_*). The remaining Rankine-Hugoniot relations connecting the left state U_l with U_{ml} via a '1-wave' and U_r with U_{mr} via a '3-wave' then mathematically constitute a system with 6 equations for the six unknowns, namely $(s_1, \rho_{ml}, v_*, p_*)$ and $(s_3, \rho_{ml}, v_*, p_*)$ with the shock speeds s_1 and s_3. In reality, not all shock solutions are physically realizable, and a rarefaction wave through which density and velocity varies smoothly occurs instead. Schematically, the Riemann problem leads to a solution as sketched in Fig. 4 consisting of a rarefaction wave, a contact discontinuity and a genuine shock. As a final note on the Euler system, a distinguishing quantity is the 'entropy' $s \equiv p\rho^{-\gamma}$, which can be shown to obey the equation

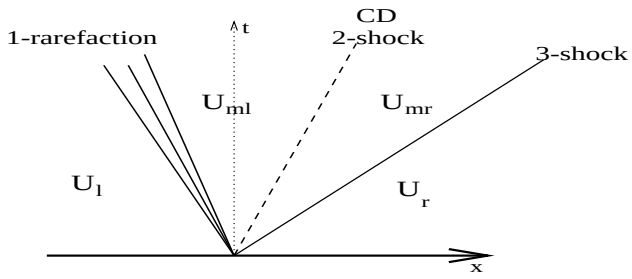

Figure 4: Schematic solution to the Riemann problem for the Euler system.

$$s_t + v s_x = 0,$$

which is not in conservation form. This equation shows that the entropy is constant along rays $\frac{dx}{dt} = v$. Through a rarefaction, the entropy will remain constant. An arbitrary entropy jump is carried by a contact discontinuity. An admissable shock will have the fluid increase its entropy as the shock passes.

III. FINITE VOLUME DISCRETIZATION

The Euler system, as well as the ideal MHD system, forms a set of nonlinear conservation laws. Written in the differential form of equations (7), the discontinuous solutions discussed above (containing shocks and contact discontinuities) seem to conflict mathematically with the implicit assumption of differentiable functions. Physically though, they correctly describe the gas dynamics in the limit of vanishing viscosity. In fact, the discontinuous solutions are perfectly allowed by the more general integral form of the conservation laws. Considering a cell $[x_1, x_2]$ and a conserved quantity ρ within this cell, the total mass in this cell changes from times t_1 to t_2 only through a flux over the cell edge $f(\rho)$ (provided that no mass sink or source exists within this

cell). This leads to the integral form

$$\int_{x_1}^{x_2} \rho(x,t_2)\,dx = \int_{x_1}^{x_2} \rho(x,t_1)\,dx + \int_{t_1}^{t_2} f(x_1,t)\,dt - \int_{t_1}^{t_2} f(x_2,t)\,dt.$$

Under the assumption of smoothly differentiable functions, and since this holds for any cell $[x_1, x_2]$ and time interval $[t_1, t_2]$, we arrive at the differential form

$$\rho_t + (f(\rho))_x = 0.$$

The Finite Volume discretization method, see [1], directly incorporates the more general integral form as follows. Given conservation laws $\mathbf{U}_t + \nabla \cdot \mathbf{F}(\mathbf{U}) = \mathbf{S}$ for the vector of conserved quantities $\mathbf{U}$ where possible sources or sinks are collected in $\mathbf{S}$, the Finite Volume method will solve for the time evolution of cell-averaged quantities U (any $\mathbf{U}$ component)

$$U_i(t) = \frac{1}{V_i}\int_{V_i} U(\mathbf{x},t)d\mathbf{x},$$

where V_i indicates the volume (length, area or true volume depending on dimensionality) of grid cell i. It therefore solves the volume averaged conservation law

$$\frac{\partial U_i}{\partial t} + \frac{1}{V_i}\sum_l \mathbf{F}_l \cdot \mathbf{n}_l = \frac{1}{V_i}\int_{V_i} S d\mathbf{x},$$

where the cell normals are $\mathbf{n}_l$. Since this is consistent with the integral form of the conservation laws, this approach is ok for dealing with discontinuous solutions as well. Note that for a 1D problem without source term, this is simply written as

$$\frac{\partial U_i}{\partial t} + \frac{1}{\Delta x_i}\left(F_{i+1/2} - F_{i-1/2}\right) = 0, \qquad (10)$$

where $F_{i+1/2}$ are fluxes defined at the cell edges. Clearly, any cell average changes only through the cell edge fluxes, and the total 'mass' in the entire discretized volume can only change through boundary losses or gains. It turns out to be extremely important to use a conservative discretization of the form (10) in order to accurately treat discontinuous (weak) solutions: schemes that can not be recasted in this form can easily produce completely erroneous shock speeds. In fact, all of the schemes (3,5,6) are conservative. E.g., the upwind flux for the advection equation is given by

$$F^{\rm up}_{i+1/2} = \frac{1}{2}\left\{v\rho_{i+1} + v\rho_i - \mid v \mid [\rho_{i+1} - \rho_i]\right\},$$

while the Lax-Friedrichs flux is

$$F^{\rm lf}_{i+1/2} = \frac{1}{2}\left\{v\rho_{i+1} + v\rho_i - \frac{\Delta x}{\Delta t}[\rho_{i+1} - \rho_i]\right\}.$$

However, as mentioned before, both schemes render first order spatial accuracy. In the Finite Volume discretization, the evaluation of fluxes at the cell edges implies that some extrapolation within the cell i is needed from the volume averaged value U_i. Simply using a constant extrapolation where $U(x \in [x_{i-1/2}, x_{i+1/2}]) = U_i$ is of course consistent with U_i as the cell average, but leads to first order accuracy where averaged edge fluxes $F_{i+1/2} = (F(U_i) + F(U_{i+1}))/2$ are used. Better, and still consistent with U_i as a volume average, is to use a linear extrapolation within the cell with slope σ_i, hence

$$U(x \in [x_{i-1/2}, x_{i+1/2}]) = U_i + \sigma_i \frac{x - x_i}{\Delta x_i}.$$

The slope is then the difference

$$\Delta U_i \equiv U_{i+1/2} - U_{i-1/2} = \sigma_i.$$

This linear reconstruction can be exploited to get a *Left* and *Right* edge centered state

$$U^L_{i+1/2} = U_i + \Delta U_i/2 \text{ and } U^R_{i+1/2} = U_{i+1} - \Delta U_{i+1}/2.$$

The flux at the cell edge then takes the average from

$$F_{i+1/2} = \left(F(U^L_{i+1/2}) + F(U^R_{i+1/2})\right)/2.$$

This process of linear reconstruction raises the spatial order of accuracy to second order.

In practice, one must limit the slopes used in the linear reconstruction in order to avoid the introduction of spurious oscillations. On comparing the slopes as obtained from using neighbouring left or right cell values, one typically needs to take the least steep slope of the two, and to fall back on constant extrapolation within a cell when these slopes conflict in sign. Schematically, this is shown in Fig. 5. Different flavours of slope limiters exist, which ensure the Total Variation Diminishing (TVD) concept. The numerical total variation is defined as the summed differences

$$\mathrm{TV} \equiv \sum\nolimits_i \mid U_{i+1} - U_i \mid,$$

and a scheme is called TVD when it ensures that this total variation diminishes with time

$$\mathrm{TV}^{n+1} \leq \mathrm{TV}^n.$$

Hence, the initial data sets a bound for the total variation at all times, and it is easily appreciated that this TVD property ensures that monotone initial data remains monotone, called 'monotonicity preserving'. In particular, since the Riemann problem is monotone, a TVD scheme automatically prevents creation of spurious oscillations.

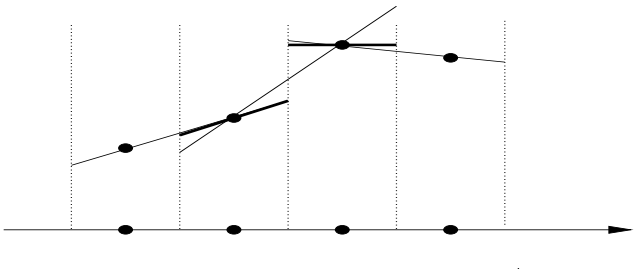

Figure 5: Slope limited linear reconstruction process.

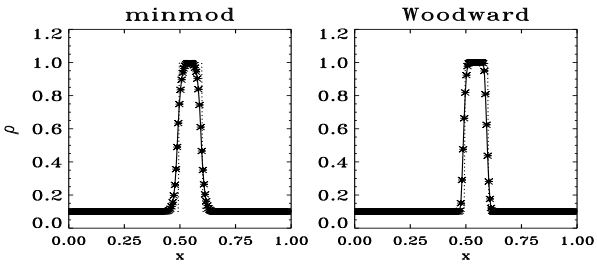

Figure 6: After one advection cycle, square pulse (initial data as dotted line) for TVDLF with minmod (left) versus Woodward (right) slope limiter.

The forward Euler one-step time marching employed in (3,5,6) would make the scheme $\mathcal{O}(\Delta t)$. Since for any explicit time marching scheme, the allowed time step Δt will be restricted by the chosen grid size Δx for numerical stability, raising the spatial order of accuracy for time-dependent simulations calls for a consistent higher order temporal accuracy. Second order can be achieved by a two-step Predictor-Corrector method

$$\mathbf{U}^{n+1/2} = \mathbf{U}^n + \frac{\Delta t}{2}\left[-\nabla\cdot\mathbf{F}(\mathbf{U}^n) + \mathbf{S}(\mathbf{U}^n)\right]$$

$$\mathbf{U}^{n+1} = \mathbf{U}^n + \Delta t\left[-\nabla\cdot\mathbf{F}(\mathbf{U}^{n+1/2}) + \mathbf{S}(\mathbf{U}^{n+1/2})\right].$$

As an explicit example, the second order Total Variation Diminishing Lax-Friedrichs scheme (TVDLF, see [2]) uses a predictor-corrector approach where the corrector step uses time centered numerical fluxes from

$$\begin{aligned} f^{n+1/2}_{i+\frac{1}{2}} &= \frac{1}{2}\Big\{F(U^L_{i+\frac{1}{2}}) + F(U^R_{i+\frac{1}{2}}) \\ &\quad - \mid c^{max}\Big(\frac{U^L_{i+\frac{1}{2}} + U^R_{i+\frac{1}{2}}}{2}\Big) \mid \left[U^R_{i+\frac{1}{2}} - U^L_{i+\frac{1}{2}}\right]\Big\}, \end{aligned}$$

where the left and right states are

$$U^L_{i+\frac{1}{2}} = U^{n+1/2}_i + \bar{\Delta U}^{n+1/2}_i/2,$$

$$U^R_{i+\frac{1}{2}} = U^{n+1/2}_{i+1} - \bar{\Delta U}^{n+1/2}_{i+1}/2.$$

The overbar denotes the slope limiter, with e.g. the 'minmod' limiter given by

$$\begin{aligned} \bar{\Delta U}_i = sgn(U_i - U_{i-1})\max\big[0, \\ \min\{\mid U_i - U_{i-1}\mid, (U_{i+1} - U_i)sgn(U_i - U_{i-1})\}\big]. \end{aligned}$$

The stencil of this TVDLF scheme is 5 cells wide, through the slope limited linear reconstruction. This scheme is generally applicable to any system of nonlinear conservation laws, by inserting the appropriate maximal physical propagation speed c^{max}. For the linear advection equation $c^{max} = v$, while for the Euler system, one would use $c^{max} = \mid v \mid + c$ consistent with (9). The first order variant of TVDLF reduces to the upwind scheme (3) for the linear advection equation, while the connection with the Lax-Friedrichs scheme is through the replacement $\mid c^{max} \mid \leftrightarrow \Delta x/\Delta t$. In Fig. 6, the periodic advection of the square pulse using the TVDLF scheme with two flavors of the slope limiters is plotted (using 200 grid points) for comparison with the MacCormack results in Fig. 3. The monotonicity preserving nature of TVDLF is evident. The nonlinearity introduced by the limiting process prevents spurious oscillations at discontinuities (essentially rendering local first order accuracy), while yielding second order accuracy on smoothly varying data.

IV. 1D MHD SIMULATIONS

Turning to ideal MHD simulations, we start in a configuration where all variables are function of the first (x) coordinate only, but vector quantities can have components perpendicular to this direction. Since we assume no variation in these other directions, the $\nabla\cdot\mathbf{B} = 0$ constraint is trivially enforced by keeping a constant x-component of the magnetic field $\bar{B}_1$. Together with the ratio of specific heats γ, there are then two parameters and in a 1.5D approach where only 1 orthogonal component is considered, the system to solve becomes a nonlinear, 5-component PDE system for the conserved quantities $(\rho, \rho v_1 \equiv m_1, \rho v_2 \equiv m_2, e, B_2)$. Its flux vector has the entries

$$\begin{array}{c} m_1 \\ \frac{m_1^2}{\rho} - \bar{B}_1^2 + (\gamma-1)(e - \frac{m^2}{2\rho}) + (2-\gamma)\frac{B^2}{2} \\ \frac{m_1 m_2}{\rho} - \bar{B}_1 B_2 \\ \frac{m_1}{\rho}\left(\gamma e - (\gamma-1)\frac{m^2}{2\rho} + (2-\gamma)\frac{B^2}{2}\right) - \bar{B}_1(\bar{B}_1\frac{m_1}{\rho} + B_2\frac{m_2}{\rho}) \\ B_2\frac{m_1}{\rho} - \bar{B}_1\frac{m_2}{\rho} \end{array}$$

The total energy now reads

$$e = \frac{p}{\gamma-1} + \frac{\rho v^2}{2} + \frac{B^2}{2}.$$

Note that we have adopted magnetic units where vacuum permeability is unity.

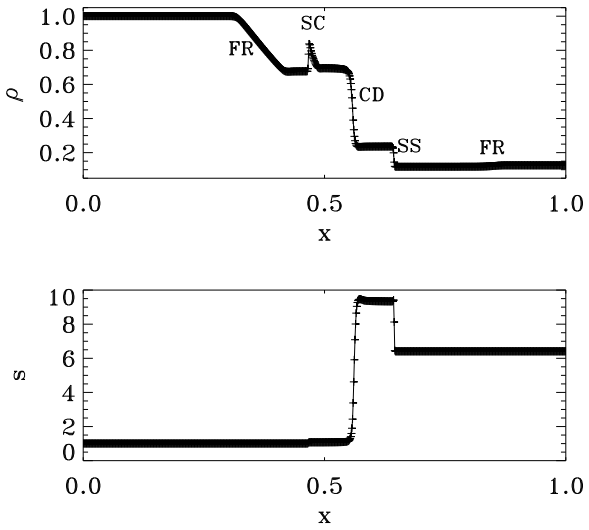

Figure 7: Density and entropy at time $t = 0.1$ for the 1.5D MHD Riemann problem.

The eigenvalues of the flux Jacobian are now v_1, $v_1 \pm c_s$, and $v_1 \pm c_f$, where the (squared) slow c_s and fast c_f magnetosonic speeds are

$$c_{f,s}^2 = \frac{1}{2}\left(\frac{\gamma p + B^2}{\rho} \pm \sqrt{\left(\frac{\gamma p + B^2}{\rho}\right)^2 - 4\frac{\gamma p}{\rho}\frac{\bar{B}_1^2}{\rho}}\right).$$

In the limit of zero B_2, one of them becomes the Alfvén speed $c_a = \bar{B}_1/\sqrt{\rho}$, while the other turns into the sound speed c. In general, the following ordering applies $c_s \le c_a \le c_f$. Including third vector components and the corresponding two additional equations for m_3 and B_3, this 1.75D system has the full 7 characteristic speeds v_1, $v_1 \pm c_s$, $v_1 \pm c_a$, and $v_1 \pm c_f$. This makes the solution of the simple Riemann problem in 1D MHD quite involved. Indeed, up to 5 signals separating 6 constant states can emerge out of two constant states in contact for 1.5D MHD, while up to 8 states form spontaneously in 1.75D Riemann problems. Two examples of a numerical solution to such 1D MHD Riemann problems are shown in Fig. 7 and 8. Fig. 7 shows the solution at $t = 0.1$ of a shock tube test from [3] where $\gamma = 2$ and $\bar{B}_1 = 0.75$. The two states are initially at rest, with left state $(\rho, p, B_2) = (1, 1, 1)$ and right state $(0.125, 0.1, -1)$. We used 800 grid points and the discontinuity was initially midway the domain $[0, 1]$. A leftward moving fast rarefaction wave (with no entropy variation), a slow compound wave, a contact discontinuity, a rightward moving slow shock, and a rightward fast rarefaction can be identified in the solution. The slow compound wave is a slow shock with a rarefaction wave attached to it, and is a possibility novel to 1D

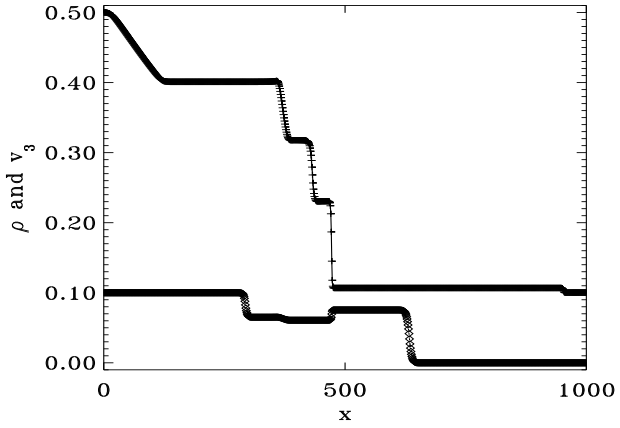

Figure 8: Density and v_3 velocity component at $t = 80$ for a 1.75D MHD Riemann problem.

compressible MHD flow: in hydrodynamics only shocks or rarefaction waves can emerge. Fig. 8 is from a 1.75D MHD simulation with parameter values $\gamma = 5/3$ and $\bar{B}_1 = 1$. The initial data separates

$$(\rho, v_1, v_2, v_3, p, B_2, B_3)_L = (0.5, 0, 1, 0.1, 1, 2.5, 0),$$

$$(\rho, v_1, v_2, v_3, p, B_2, B_3)_R = (0.1, 0, 0, 0, 0.1, 2, 0),$$

with the transition at $x = 350$. We use 1000 grid cells of unit size. Shown is the density and the velocity component v_3 at time $t = 80$, and from left to right one encounters the following features: fast rarefaction wave, Alfvén signal, slow rarefaction, contact discontinuity, slow shock, Alfvén signal, fast shock.

V. MULTI-D MHD AND $\nabla \cdot \mathbf{B} = 0$

Conceptually, multi-D simulations can be reduced to a succession of 1D problems in the various coordinate directions. Strang type dimensional splitting for a 2D case writes

$$\mathbf{U}^{n+1} = L^x_{\Delta t/2} L^y_{\Delta t} L^x_{\Delta t/2} \mathbf{U}^n,$$

where the operator $L^x_{\Delta t/2}$ indicates an update with a timestep $\Delta t/2$ taking account of only the fluxes in the x-direction. Alternatively, we can alternate coordinate directions as

$$\mathbf{U}^{n+2} = L^x_{\Delta t} L^y_{\Delta t} L^y_{\Delta t} L^x_{\Delta t} \mathbf{U}^n.$$

For multi-D MHD simulations, we also need to handle the non-trivial $\nabla \cdot \mathbf{B} = 0$ constraint. This is because even if it is satisfied exactly at $t = 0$, one can numerically generate $\nabla \cdot \mathbf{B} \neq 0$ due to the non-linearities of the

various shock-capturing methods. Besides the fact that this is clearly undesirable physically, it can even cause fatal numerical instabilities. However, exact solenoidal fields may not be needed in numerical simulations, as one always faces discretization and machine precision errors. In practice, it turns out to be very difficult (although possible [4]), to insist on (1) a conservative form – which is needed for correctly handling shocks, (2) ensure solenoidal $\mathbf{B}$ in some discrete sense, *and* (3) have the discretized Lorentz force orthogonal to the magnetic field in the cell centers. The conservative form of the MHD equations uses the divergence of the Maxwell stress tensor, which is equal to the Lorentz force provided $\nabla \cdot \mathbf{B} = 0$ since

$$\nabla \cdot \left(\mathcal{I} \frac{B^2}{2} - \mathbf{B}\mathbf{B} \right) = -(\nabla \times \mathbf{B}) \times \mathbf{B} - \mathbf{B} \left(\nabla \cdot \mathbf{B} \right).$$

Many strategies to cope with the solenoidal constraint have been developed. A thorough comparison of 7 different strategies on a series of 9 2D MHD tests can be found in [5]. Here, we only mention the projection scheme strategy, which controls the numerical value of $\nabla \cdot \mathbf{B}$ in a particular discretization to a given accuracy. The basic idea [6] is to correct the $\mathbf{B}^*$ computed by a scheme with $\nabla \cdot \mathbf{B}^* \neq 0$, by projecting it on the subspace of zero divergence solutions. Hence, we modify $\mathbf{B}^*$ by subtracting the gradient of a scalar field ϕ, to be computed from

$$\nabla^2 \phi = \nabla \cdot \mathbf{B}^*. \tag{11}$$

By construction, this yields a solenoidal $\mathbf{B} = \mathbf{B}^* - \nabla\phi$ which is then used in the next timestep. This process can be repeated after each time step. It is important to note that the accuracy up to which the Poisson problem (11) is solved need not be machine precision, and that this approach keeps the order of accuracy of the base scheme, while not violating its conservation properties.

With a strategy for handling the divergence of $\mathbf{B}$ in place, we can now turn to multi-D simulations of the conservative ideal MHD equations:

$$\begin{aligned} \rho_t + \nabla \cdot (\mathbf{v}\rho) &= 0 \\ (\rho\mathbf{v})_t + \nabla \cdot (\mathbf{v}\rho\mathbf{v} - \mathbf{B}\mathbf{B}) + \nabla p_{tot} &= 0 \\ e_t + \nabla \cdot (\mathbf{v}e + \mathbf{v}p_{tot} - \mathbf{B}\mathbf{B} \cdot \mathbf{v}) &= 0 \\ \mathbf{B}_t + \nabla \cdot (\mathbf{v}\mathbf{B} - \mathbf{B}\mathbf{v}) &= 0, \end{aligned}$$

where we used the total pressure $p_{tot} \equiv p + B^2/2$. As an instructive example from [7], we perform a 2D MHD simulation on $(x, y) \in [-0.5, 0.5]^2$, where we locally perturb a homogeneous magnetized plasma at rest. Taking $\gamma = 5/3$, $\rho = 1$, $p = 0.6$ and a uniform horizontal $\mathbf{B} = 0.9\hat{e}_x$ (making the sound speed $c = 1$, Alfvén speed $c_a = 0.9$), we perturb 4 cells at the origin with a 10 % pressure and density increase. We used a non-uniform 300^2 grid, and show in Fig. 9 the resulting total pressure field. Overplotted is the theoretical Friedrichs group diagram which should emerge out of a δ-function perturbation. The fast magnetosonic waves propagate non-spherically outwards in all directions, traveling faster in the direction perpendicular to $\mathbf{B}$. The slow magnetosonic signals are the extremely anisotropic cusp-like features. On top of what is seen in Fig. 9, the entropy signal of the initial perturbation remains stationary at the origin.

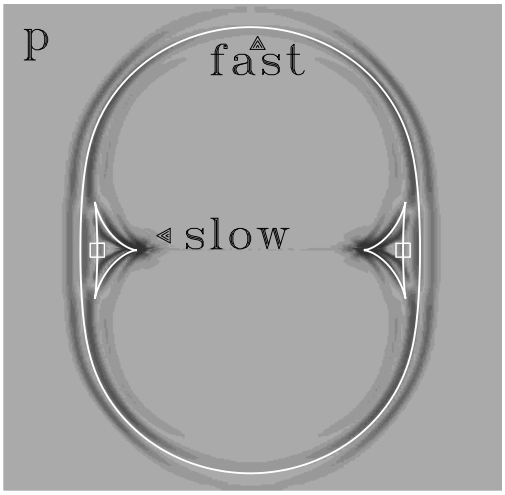

Figure 9: The total pressure in a locally perturbed homogeneous plasma shows the fast and slow wavefronts.

A representative 2D MHD simulation where a shock-dominated transition to MHD turbulence occurs can be taken from [8]. A doubly periodic domain $[0, 2\pi]^2$ is initialized with a uniform $\rho = 25/9$, $p = 5/3$ while $\gamma = 5/3$. A velocity vortex given by $\mathbf{v} = (-\sin y, \sin x)$ then corresponds to a Mach 1 rotation cell, and magnetic islands of half the horizontal wavelength of the velocity roll are superimposed as $\mathbf{B} = (-\sin y, \sin 2x)$. Shown in Fig. 10 is the temperature $T = p/\rho$ at time $t = 3.14$ which clearly shows how the ensueing dynamics is an intricate interplay of shock formations and collisions.

VI. KELVIN-HELMHOLTZ INSTABILITY AND INDUCED RECONNECTION

We conclude with a recent result from grid-adaptive [9], high-resolution, resistive MHD simulations [10]. Resistive MHD augments the ideal system with Ohmic heating in the energy equation and relaxes the frozen-in condition of the induction equation, allowing topological reconfigurations of $\mathbf{B}$. The study

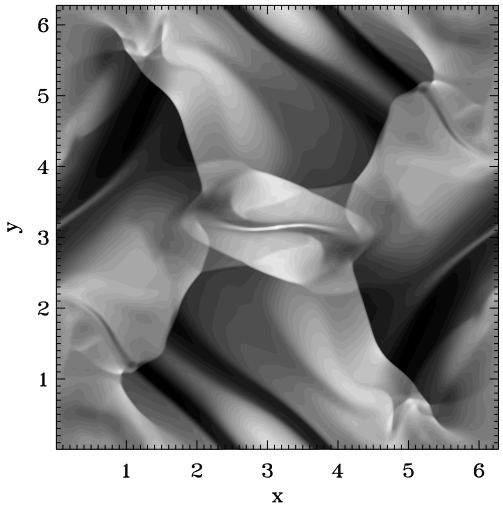

Figure 10: Temperature at $t = 3.14$ in a shock-dominated transition to compressible MHD turbulence.

considers the nonlinear evolution of a uniformly magnetized, 2D shear flow configuration where $v_x(y) = \frac{1}{2}V \tanh 20y$, for a transonic $V/c = 1$ flow. The initial plasma beta, measuring the ratio of thermal to magnetic pressure, is equal to $\beta = 1080$, so that the initial evolution is essentially hydrodynamic in nature. For several sound crossing times, the magnetic field is merely passively advected by the developing vortical flows. The latter set in due to the Kelvin-Helmholtz instability of the shear flow configuration. Note how the density evolution depicted in Fig. 11 shows the coalescence of vortices: the most unstable mode has a wavelength which is consistent with 8 vortices being formed at early times. At about $t = 10$ we see the local effect of sufficiently amplified magnetic fields, which have been dragged about by consecutive mergers. Locally anti-parallel field regions are forced together in the process, leading to induced reconnection through tearing-type resistive instability events, forming small magnetic and density islands. This was previously found to occur in cospatial current-vortex sheets [11]. This eventually causes a rapid transition to MHD small-scale turbulence, while the trend to large-scale coalescing continues simultaneously.

Summarizing, numerical MHD simulations can significantly advance our understanding of non-linear fundamental plasma physical magneto-fluid dynamics.

ACKNOWLEDGMENTS

This work is supported by the contract of Association between Euratom/FOM, within the framework of the European Fusion Programme. Opinions expressed herein do not necessarily reflect those of the EC.

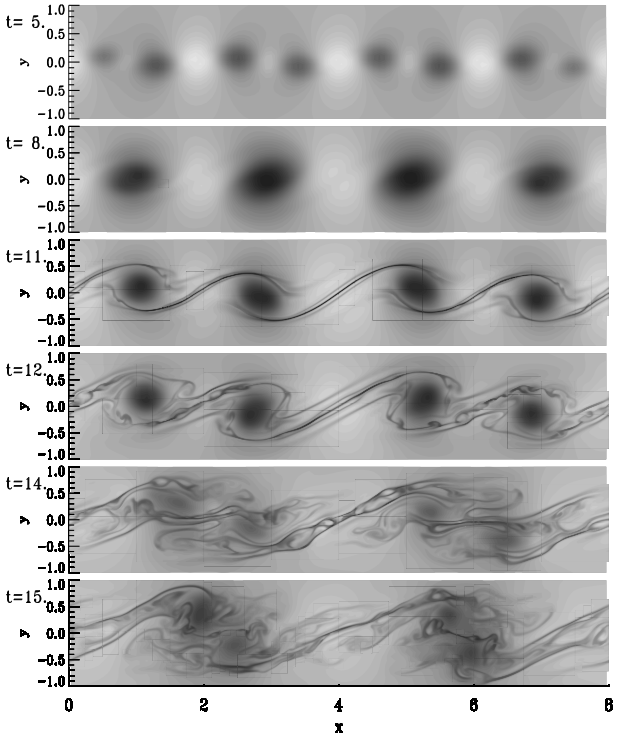

Figure 11: Density evolution in a 2D MHD shear flow layer. Note the large-scale coalescence by vortex pairing, and the small island formation through induced reconnection. This leads to MHD turbulence.

REFERENCES

1. R.J. Leveque, *Finite volume methods for hyperbolic problems*, Cambridge University Press, 2002
2. G. Tóth, D. Odstrčil, *JCP* **128**, 82 (1996)
3. M. Brio, C.C. Wu, *JCP* **75**, 400 (1988)
4. G. Tóth, *JCP* **182**, 346 (2002)
5. G. Tóth, *JCP* **161**, 605 (2000)
6. J.U. Brackbill, D.C. Barnes, *JCP* **35**, 426 (1980)
7. R. Keppens, in: *Parallel Computational Fluid Dynamics – Trends and Applications*, C.B. Jenssen et al. (eds.), Elsevier Science B.V., 31 (2001)
8. J.M. Picone, R.B. Dahlburg, *Phys. Fluids B***3**, 29 (1991)
9. R. Keppens et al., *CPC* **153**, 317 (2003)
10. H. Baty et al., *Phys. of Plasmas*, submitted 2003
11. R. Keppens et al., *J. Plasma Ph.* **61**, 1 (1999)